



# Ethanol droplet formation, dynamics and combustion mode in the flame of the SpraySyn-nozzle

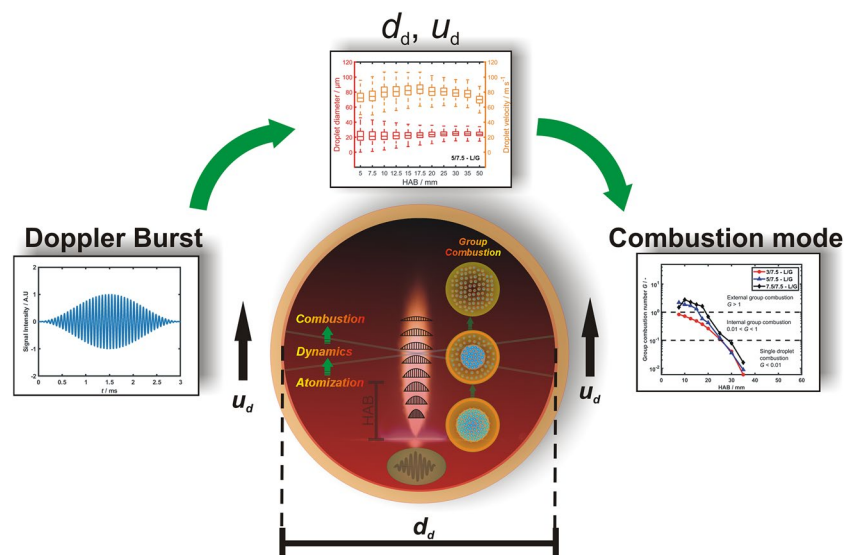
Malte F. B. Stodt<sup>1,2</sup> · Johannes Kiefer<sup>2,3</sup> · Udo Fritsching<sup>1,3,4</sup>

Received: 22 March 2019 / Revised: 2 June 2019 / Accepted: 3 July 2019 / Published online: 15 July 2019  
© Springer-Verlag GmbH Germany, part of Springer Nature 2019

## Abstract

The synthesis of nanoparticles via flame spray pyrolysis (FSP) is based on a couple of physicochemical steps such as precursor atomization, droplet evaporation, fuel combustion, particle nucleation and growth. Most recent studies on FSP are focused on the particle formation without taking the antecedent precursor atomization and spray formation into account. In the present work, the atomization characteristics under burning and non-burning conditions are investigated by means of laser sheet Mie-scattering images and phase Doppler anemometry. The influence of the gas to liquid volume ratio on the spray formation, jet morphology and scales of turbulence in the nozzle far-field are studied to assess the performance of the external-mixing gas-assisted SpraySyn-nozzle. The turbulent flame spray is characterized by the Kolmogorov length scale and the Kolmogorov shear rate. The droplet–droplet interaction and group combustion behaviour, enabling clouds of merely vaporizing droplets surrounded by a flame sheath, are investigated. The experimentally determined droplet velocities, turbulence length scales and the analysis of group combustion modes allow a deeper insight into the spray flame dynamics and droplet mixing zones.

## Graphic abstract



✉ Malte F. B. Stodt  
m.stodt@iwt.uni-bremen.de

<sup>1</sup> Leibniz Institute for Materials Engineering IWT,  
Badgasteiner Str. 3, 28359 Bremen, Germany

<sup>2</sup> Technische Thermodynamik, University of Bremen,  
Badgasteiner Str. 1, 28359 Bremen, Germany

<sup>3</sup> MAPEX Center for Materials and Processes, University  
of Bremen, Am Fallturm 1, 28359 Bremen, Germany

<sup>4</sup> Department of Process and Chemical Engineering,  
University of Bremen, Bibliothekstr. 1, 28359 Bremen,  
Germany

## 1 Introduction

The flame spray pyrolysis (FSP) is an established technique for the synthesis of tailored inorganic nanoparticles with a broad spectrum of liquid and solid metal-based precursors available. Many metal and semi-conductor elements of the periodic table can be turned into nanosized metal oxides and mixed metal oxides within the flame spray. Such nanomaterials are of special interest for many applications since they offer unique properties, such as large active surface areas for catalysis (Mädler et al. 2002; Kelesidis et al. 2017), and special thermoelectric (Petermann et al. 2011) and supermagnetic properties (Teja and Koh 2009; Schlleier et al. 2016). Furthermore, nanomaterials provide mechanically, chemically and electrically stable structures that are of high interest in energy-related applications such as batteries, supercapacitors and highly efficient electrocatalysts (Hamid et al. 2012; Meierhofer et al. 2017).

To tap the full potential of nanosized metal oxides, the conditioning of mixing zones within the spray flame (atomization, evaporation, and particle nucleation) is necessary to successfully design materials and tailor their morphology, composition, and crystallinity. Substantial insights into the spray formation and fluid flow are necessary to control the droplet evaporation and reaction kinetics. However, optical spray diagnostics inside dense sprays and the near-field of the atomizing spray is challenging owing to multiple scattering effects (Bachalo 2000; Berrocal 2006; Linne et al. 2009). For spray diagnostics in dense sprays like in FSP with droplet number densities of the order of  $\approx 10^3 \text{ # cm}^{-3}$ , the phase Doppler anemometry (PDA) is a proven measurement technique as it provides high resolution and time-resolved single droplet diameter and velocities even in dense sprays (Bachalo 2000; Strakey et al. 2000).

During the last decades, several external-mixing gas-assisted nozzles have been investigated for FSP using anemometry methods. Tikkanen et al. (1997) investigated the flow fields of droplets of isopropanol with dissolved manganese- and aluminium-based precursors using a custom-made two-fluid nozzle. They measured velocities as high as  $160 \text{ m s}^{-1}$  using laser Doppler velocimetry. Heine and Pratsinis (Heine and Pratsinis 2005) investigated the droplet dynamics of zirconium *n*-propoxide and ethanol droplets, which were atomized using a Schlick-nozzle. Their PDA measurement revealed gas velocities up to  $140 \text{ m s}^{-1}$ . Heine et al. (Heine et al. 2006) furthermore studied the gas entrainment and the turbulent flow field in axial direction downstream a Schlick-nozzle. The highest reported gas velocities in FSP, to the best of our knowledge, were measured by Gröhn et al. reaching velocities up to  $184 \text{ m s}^{-1}$  using a custom-made pilot FSP two-fluid nozzle (Gröhn et al. 2012).

Besides the fluid flow characteristics of gas-assisted nozzles, Eslamian and Heine (2008) also investigated the combustion of the spray flame by means of the group combustion theory of Chiu and Liu (1977). This theory takes the interaction of droplets in groups into account, as they consider changes of the local ambient environment by means of a decreasing heat transfer and mass transfer rate (Chiu and Liu 1977; Sirignano 1983). They found out that large turbulence intensities favor the mixing of the droplets and the oxidizer and thus enhance the formation of homogeneous nanoparticles by FSP. Rosebrock et al. and Li et al. investigated the isolated burning of multicomponent droplets and described a mechanism of single droplets that disintegrate through cascade-like microexplosions and further promote the formation of homogeneous nanoparticles by single droplet combustion (Rosebrock et al. 2016; Li et al. 2017). Sornek et al. (2000) also investigated the effect of turbulence on combustion in a similar environment. They found out that turbulence parameters strongly influence the evaporation rate of fuels since droplet interactions are reduced and the average spacing between single droplets is increased.

The SpraySyn-burner (Schulz et al. 2018) has been developed as an atomization reference with specific gas supplies using a sintered bronze matrix and non-critical dispersion gas flow conditions enabling the control of reaction conditions and simulation-friendly boundary conditions. To define standard operation conditions for the SpraySyn-burner, a comprehensive database for model development and standardized in situ experiments are required. The primary and secondary breakups of precursor solutions and the scales of turbulence are a predeterminating step and consequently control the mixing, evaporation and reaction zones of the spray.

The purpose of the present study is to determine atomization characteristics and flow structures of the SpraySyn-burner (Schulz et al. 2018) in dense and diluted spray zones using an ethanol spray. A turbulence analysis aims at providing a deep insight into the structure and shear stresses in the spray flame to be used for the validation of computational spray flame models. Furthermore, the prediction of the group combustion mode according to Chiu and Liu (1977) is presented to identify the different combustion regimes. This supports the choice of adequate feed rates for homogeneous nanoparticle synthesis.

## 2 Methods

### 2.1 Experimental methodology

The experiments were carried out with the stainless steel external-mixing gas-assisted SpraySyn-burner (Schulz

et al. 2018) as illustrated in Fig. 1. The dispersion gas (7.5 L min<sup>-1</sup> O<sub>2</sub>) and pilot gas (2 L min<sup>-1</sup> CH<sub>4</sub>, 5 L min<sup>-1</sup> O<sub>2</sub>) are controlled with calibrated mass flow controllers (Bronkhorst High-Tech B.V., Ruurlo, The Netherlands). The liquid feed is supplied using a high-precision syringe pump (KDS Scientific, Holliston, USA). The fluid is injected through a concentric capillary tube (inner diameter = 400 μm, outer diameter = 750 μm), which protrudes 0.5 mm above the rest of the annular gap of the dispersion gas. The size of the annular gap for the dispersion gas exhibits a cross-sectional area of 1.38 mm<sup>2</sup>. The annular gap is further surrounded by a concentric premixed pilot flame. Additional sheath gas (N<sub>2</sub>) is fed through a sintered bronze matrix with a volume flow of 130 L min<sup>-1</sup> to stabilize the flame.

### 2.2 PDA

Droplet size and velocity distributions of an ethanol spray (ethanol absolute, Lot: 176124009, VWR Chemicals, Radnor, USA) are determined using a one-dimensional phase Doppler Anemometer (BSA 6000, Dantec Dynamics A/S, Tonsbakken, Denmark). For the fiber-optic-based system, a detection angle of 30° was chosen to detect first-order refracted light and to avoid ambiguities from different diffraction orders. A water-cooled 5W argon-ion laser (Innova 70c, Coherent Inc., USA) is operated generating a blue laser beam with a wavelength of λ = 488 nm. The laser beam is introduced into a transmitter box (FiberFlow, Dantec Dynamics A/S, Tonsbakken, Denmark) and split into two frequency-shifted (Δf = 45 MHz) laser beams. The ellipsoidal measurement volume formed by the two intersecting laser beams has a diameter of 0.5 mm, a length of 1.4 mm, and is kept constant during the experiments since the size

range of droplets did not vary significantly. Large intersection angles θ of the emitting laser beams impede measurements very close to the nozzle tip due to the geometry of the burner (radius ~ 95 mm). Hence, the focal length F of the emitting optics is set to F = 1000 mm to facilitate measurements down to heights above the burner (HAB) of HAB = 5 mm. The settings are summarized in Table 1. The sample size at each measurement location is 20,000 droplets. The optical thickness τ<sub>0</sub> (Coghe and Cossali 2012; Linne et al. 2009) of the cold ethanol spray lies throughout the whole axial centerline of the spray within the single scattering regime (0.07 ≤ τ<sub>0</sub> ≤ 0.16) and measurement errors caused by multiple scattering are negligible (Berrocal 2006; Linne et al. 2009). The SpraySyn-burner is positioned by a two-dimensional traversing system (Dantec Dynamics A/S, Tonsbakken, Denmark) controlled by a stepping motor.

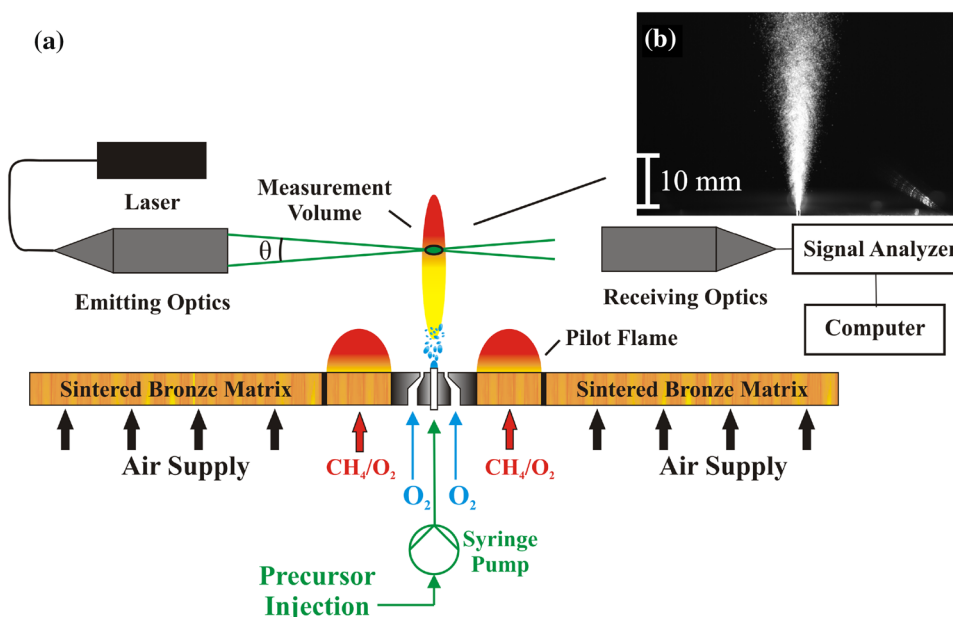
### 2.3 Turbulence analysis

The scale of turbulence of the ethanol spray is estimated using the experimentally determined droplet velocity distributions from PDA measurements along the axial centerline of the spray. The dimensionless turbulence intensity T<sub>u</sub> is defined as the ratio between the root mean square (RMS) velocity fluctuations, u<sub>RMS</sub>, and the arithmetic average velocity  $\bar{u}$

$$T_u = \frac{u_{RMS}}{\bar{u}}. \tag{1}$$

Temporally irregular resolved data sequences (time-series) measured by PDA were used to calculate the temporal auto-correlation function (ACF) of the continuous phase velocities u and were corrected employing a

**Fig. 1** **a** Schematic of the experimental setup for droplet size and velocity measurements of cold and flame spray for nanoparticle synthesis using PDA; **b** droplet phase of a cold spray visualized by laser sheet imaging



linear-interpolation approach to obtain uniform time steps  $\Delta t$ . The normalized ACF  $R_r(\tau_k)$  for  $N$  data points is given by

$$R_r(\tau_k) = \frac{1}{N} \frac{\sum_{i=1}^{N-k} (u_i - \bar{u})(u_{i+k} - \bar{u})}{(u_{\text{RMS}})^2}, \quad (2)$$

with  $k = 0, \dots, K$ , where  $K$  is the number of time lags  $\tau_k$ ; hence,  $K = N - 1$ . The integral turbulence timescale  $t_I$  is defined by the integral of  $R_r(\tau_k)$  as

$$t_I = \int_0^\infty R_r(\tau_k) d\tau \quad (3)$$

and is solved up to the first zero-axis crossing using trapezoidal numerical integration. The accuracy of the integral timescale depends on the resolution of the ACF up to the first zero-axis crossing, which is the case when the data rate is much higher than the correlated timescale. In the spray examined in this work, this was not always achieved. Therefore, only data with a resolution of at least eight data points of the ACF before first zero-axis crossing are used. The length scale of the turbulence is consequently calculated by

$$L_I = t_I u_{\text{RMS}}. \quad (4)$$

Assuming isotropic flow and Taylor hypothesis, the turbulent dissipation rate  $\varepsilon$  is defined by

$$\varepsilon = 0.8 \frac{(u_{\text{RMS}})^3}{L_I}. \quad (5)$$

Corresponding to Kolmogorov's theory (Tennekes and Lumley 1972) the statistics of the small-scale motions is uniquely dependent on the dissipation rate  $\varepsilon$  and the temperature-dependent fluid kinematic viscosity  $\nu(T)$ . Hence, the Kolmogorov turbulence length scale  $\eta$  and shear rate  $\Gamma$  are defined as

$$\eta = \left( \frac{\nu(T)^3}{\varepsilon} \right)^{(1/4)} \quad (6)$$

$$\Gamma = \left( \frac{\varepsilon}{\nu(T)} \right)^{(1/2)}. \quad (7)$$

**Table 1** PDA-setup settings for droplet size and velocity measurements

Wavelength $\lambda$	488 nm
Emitting optic $F$	1000 mm
Receiving optic $F$	500 mm
Frequency shift	45 MHz
Bandwidth	50 MHz
Number of photomultipliers	3
Photomultiplier voltage	800 V
Fringe direction	Negative

The fluid kinematic viscosity was estimated to be  $\nu = 4.2 \times 10^{-4} \text{ m}^2 \text{ s}^{-1}$ , assuming air at  $T = 2000 \text{ K}$ . The power spectral density is calculated applying a fast Fourier transformation (FFT) to the ACF.

## 3 Results and discussion

### 3.1 Atomization

High-speed camera imaging (HSCI) illustrates the atomization phenomena taking place several millimeters above the nozzle tip as a preliminary step before flame spray formation. The atomization mechanisms taking place in our measurements are assumed to be a combination of liquid–gas aerodynamic interactions that are governed by the following four forces: gravity force, inertia, surface tension force, and viscous forces (Sirignano and Mehring 2000). The high-speed images for a cold  $5 \text{ mL min}^{-1}$  ethanol spray are shown in Fig. 2 with increasing gas to liquid ratio for dispersion gas flow rates from  $3.0$  to  $20.0 \text{ L min}^{-1}$ . For a dispersion gas flow rate of  $3.0 \text{ L min}^{-1}$ , the formation of a coherent liquid core with surface deformation and ligaments is observed. With increasing dispersion gas flow rate up to  $7.5 \text{ L min}^{-1}$ , large liquid structures formed above the capillary tip enhancing permanent recirculation zones that form lamellas. These lamellas further disintegrate into smaller droplets by waving, before they undergo catastrophic breakup. The location of the recirculation zone was observed on the left side of the tip, causing a slight radial shift of the atomization zone to the right side including the formation of lamellas for dispersion gas flow rates of  $12.5 \text{ L min}^{-1}$ . For distances larger than  $1 \text{ mm}$  above the nozzle tip, the formation of a fine homogeneous spray through catastrophic breakup is observed. Using FSP, deflection of larger lamella and temporal recirculation zones may enhance the formation of large hollow nanoparticles by incomplete precursor evaporation.

### 3.2 Flame spray structure

Images of the liquid phase under reacting conditions are acquired using laser sheet Mie-scattering (LSMS) of droplets generated from a single laser pulse ( $\Delta t = 7 \text{ ns}$ ), expanded into a thin sheet, passing the axial centerline of the spray. Using a high-speed camera (FASTCAM SA4, Photron, Tokyo, Japan) with an exposure time of  $t = 99 \mu\text{s}$  (shutter speed =  $1/10,000$ ), an instantaneous view of the droplet field within the flame spray is enabled since flame luminosity is not visible at this gating time. Figure 3 shows single images with four different ethanol feed rates of  $1.5, 3, 5, \text{ and } 7.5 \text{ mL min}^{-1}$ . A large jet core is formed in the dense spray region. High droplet concentrations occur along the center axis of

the spray and smaller droplets, likely lamella, are deflected towards the spray boundaries. It is found that the length of the dense spray region and the diameter of the spray core are increasing with the liquid feed rate since more liquid is atomized and evaporated using the same dispersion gas flow and pilot flame gas flow. Visualizing these different droplet fields at varying feed rates, it can be deduced that different droplet group combustion modes may prevail in different spray regions.

### 3.3 PDA measurements

In this section, droplet size and velocity profiles of an ethanol spray under burning and non-burning conditions for liquid feed rates of 3, 5, and 7.5 mL min<sup>-1</sup> at a constant dispersion gas flow of 7.5 L min<sup>-1</sup> oxygen are presented. The burning and non-burning conditions are investigated along the axial centerline.

#### 3.3.1 Droplet concentration

The droplet sampling rate, which is exemplarily shown in Fig. 4, indicates the local droplet concentration and elucidates the different spray regions for both, burning and non-burning spray. For the cold spray and the flame spray, an increasing data rate is detected with increasing distance up to HAB = 15 mm. This region of the spray is mainly governed by primary and secondary breakups and ongoing formation of spherical single droplets. It should be noted that nonspherical droplets are not processed by the PDA processor leading to inevitable measurement errors. The spherical validation of the detected droplets throughout the whole measurements lies in the range from 77.6% (HAB = 5 mm) to 99.5% (HAB > 20 mm), thus nonspherical droplets have not been taken into account. For larger distances from the nozzle, i.e., HAB > 15 mm, the data rate of the cold spray maintains a constant value of ≈ 5 kHz, indicating a homogeneous spray field. The flame spray shows a distinctive decrease of the data rate with increasing distance, resulting in a data rate of ≈ 300 Hz at HAB = 50 mm. This

reduction of the data rate is caused by the evaporation of small droplets, as also indicated in Fig. 3.

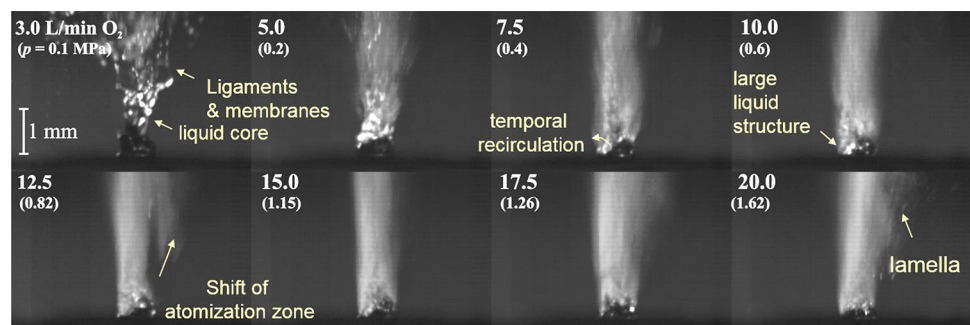
#### 3.3.2 Droplet size

Figure 5a, b shows the arithmetic mean droplet diameter  $\bar{d}_d$  under non-burning and burning conditions, respectively. Corresponding to Heine and Pratsinis (2005), both sprays can be distinguished into two regions. The breakup region is located up to HAB = 10 mm and is characterized by a sharp decrease of  $\bar{d}_d$  owing to secondary breakup and the formation of spherical single droplets.

In the breakup region of the cold spray, initial mean diameters of 46 μm are detected at HAB = 5 mm, which are then reduced along the centerline by secondary breakup to mean diameters between 18 and 25 μm at HAB = 10 mm. For the flame spray, much smaller initial droplet sizes and similar droplet sizes downstream are measured in comparison to the cold spray, reaching from initial mean diameter of 25 μm at HAB = 5 mm down to 20 μm at HAB = 10 mm. According to Heine and Pratsinis (2005), the second spray region is related to the evaporation region and is located at HAB > 10 mm. Within this region, the spray is fully developed and an increase in the mean droplet diameter can be observed. Here, more than 97.1% of the detected droplets have been found to be spherical. For the cold spray, this increase in  $\bar{d}_d$  is caused by the fast evaporation of small droplets created by catastrophic breakup and converging–diverging droplet trajectories that facilitates droplet coalescence. For HAB > 25 mm, a slight decrease of  $\bar{d}_d$  is observed owing to further droplet evaporation and radial droplet deflection of smaller droplets following the turbulence of the gas flow. The increase of the ethanol feed rate from 3 to 7.5 mL min<sup>-1</sup> results in an increase of the mean droplet diameter of about 6 μm at HAB = 15 mm.

For the flame spray, the evaporation region is characterized by a distinctive increase in  $\bar{d}_d$ . This increase in  $\bar{d}_d$  is mainly caused by the fast evaporation of small droplets. The increase of the ethanol feed rate from 3 to 7.5 mL min<sup>-1</sup> results in a droplet diameter increase of 3 μm at HAB = 20 mm. Figure 6 shows the evolution of the

**Fig. 2** High-speed images of the ethanol droplet breakup at constant liquid feed rate of 5 mL min<sup>-1</sup> with increasing dispersion gas flow rate from 3.0 to 20.0 L min<sup>-1</sup> under non-reacting conditions. The increase of the dispersion gas causes an increasing pressure drop since the outlet area is not adjusted, facilitating the atomization



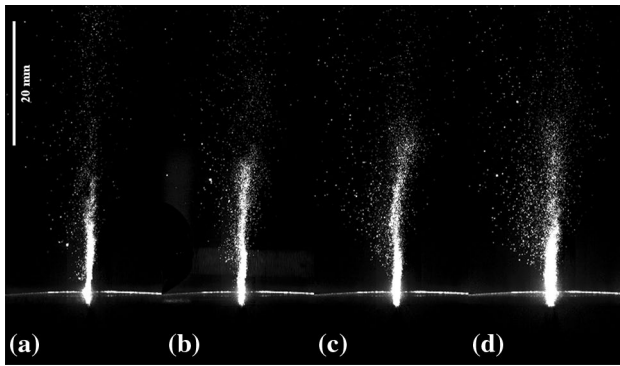


**Fig. 3** Single-laser sheet Mie-scattering images of the droplet-laden fraction. **a** 1.5/7.5—L/G; **b** 3/7.5—L/G; **c** 5/7.5—L/G; **d** 7.5/7.5—L/G (1.5/7.5—L/G refers to 1.5 mL min<sup>-1</sup> ethanol and 7.5 L min<sup>-1</sup> oxygen)

normalized droplet size distribution along the axial centerline of the spray for 10 mm < HAB < 50 mm. A distinctive shift of the size distribution towards larger mean diameter caused by evaporation and deflection of small droplets can be observed. This is also observed in Fig. 7a, b, where the width of the droplet size distribution is indicated by the boxes and the bars. The droplet distributions are all monomodal and corresponding to a Rosin–Rammler spread parameter of  $q = 1.79$  and  $q = 2.73$  for the cold spray and the flame spray (HAB = 10 mm), respectively. According to Lefebvre and McDonnell (2017), values of  $q > 2$  correspond to a uniform spray. At most locations, droplet sizes in the range of 1–4  $\mu\text{m}$  are present, serving as tracer particles (Heine et al. 2006). Droplets smaller than 4  $\mu\text{m}$  are extracted from the PDA data and are used

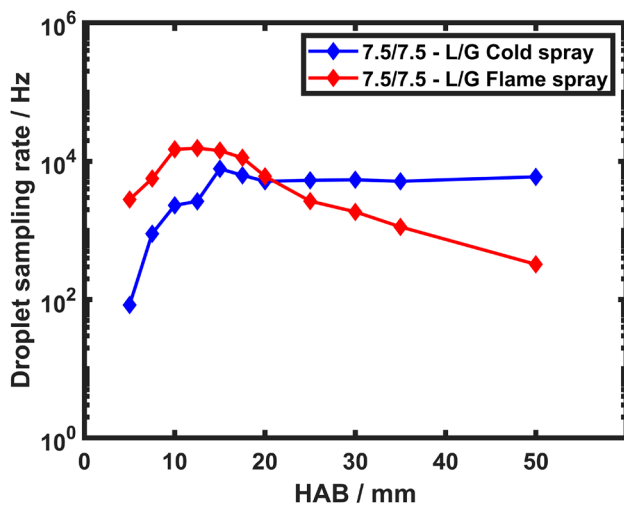


**Fig. 4** Droplet sampling rate along the axial centerline of the ethanol spray for cold and flame spray

to estimate the flame gas velocity and cold gas velocity in the next section.

### 3.3.3 Droplet and gas velocity

The droplet velocities of the ethanol spray along the centerline are shown in Fig. 5c, d for the non-burning and burning spray with maxima of 83 m s<sup>-1</sup> and 96 m s<sup>-1</sup>, respectively. The respective evolution of the droplet velocity distributions (5/7.5—L/G) are shown in Fig. 7a, b. While the width of the droplet velocity distribution of the cold spray is constant, the velocity distribution in the flame spray is slightly narrowed with increasing HAB owing to the fast droplet evaporation. The droplet velocity of the non-burning ethanol spray initially accelerates after atomization by the dispersion gas up to its maximum velocity at HAB = 10 mm. Further downstream, the droplet velocity rapidly decreases linearly owing to friction, gravity and radial jet expansion. It is found that the maximum spray velocity is decreased at increasing the feed rate from 3 to 7.5 mL min<sup>-1</sup> by 20 m s<sup>-1</sup>. In contrast, the acceleration of the burning spray is much more intense and takes more time to reach maximum velocity (non-burning spray:  $\sim 150 \mu\text{s}$ ; burning spray:  $\sim 230 \mu\text{s}$ ). This is caused by rapid release of additional vaporized species and subsequent

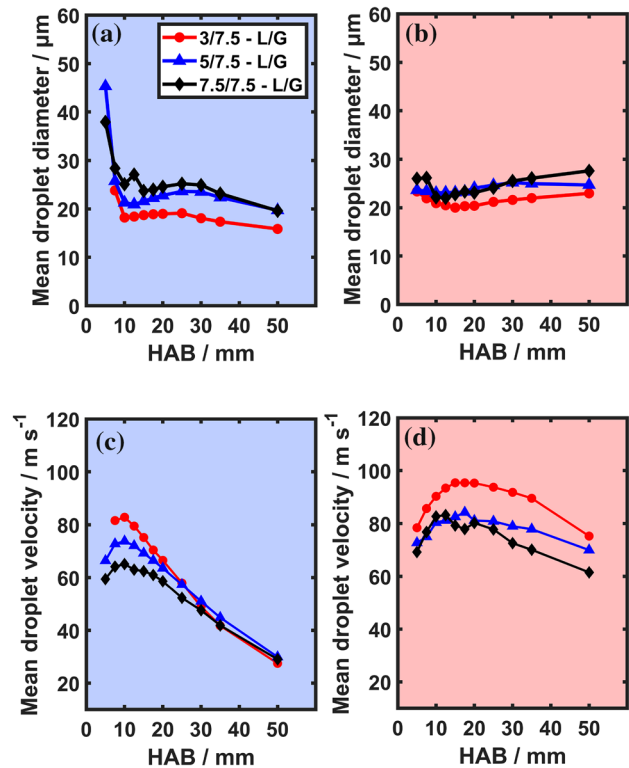


**Fig. 5** Arithmetic mean droplet size and mean droplet velocities of an ethanol spray measured along the axial centerline under non-burning (**a**, **c**) and burning (**b**, **d**) conditions for liquid feed rates (L) of 3, 5, and 7.5 mL min<sup>-1</sup> and 7.5 L min<sup>-1</sup> oxygen as dispersion gas (G)

thermal gas expansion from ethanol, with a combustion enthalpy of  $-1367.57 \text{ kJ mol}^{-1}$  at standard conditions (Chao and Rossini 1965), facilitating higher velocities.

Figure 8 shows the gas velocities along the centerline of the spray for both, reacting and non-reacting sprays, that are extracted from droplets in the size range of  $1 \mu\text{m} \leq d_d \leq 4 \mu\text{m}$ . In general, the flame gas reaches velocities that are up to  $50 \text{ m s}^{-1}$  higher than the gas in the cold spray. In the dense spray region, the flame gas is accelerated by the rapid release of vapor from combustion and reaches maximum velocities as high as  $110 \text{ m s}^{-1}$ . This acceleration is not observed in the cold spray since no significant vapor release and no thermal expansion occur. Furthermore, it is

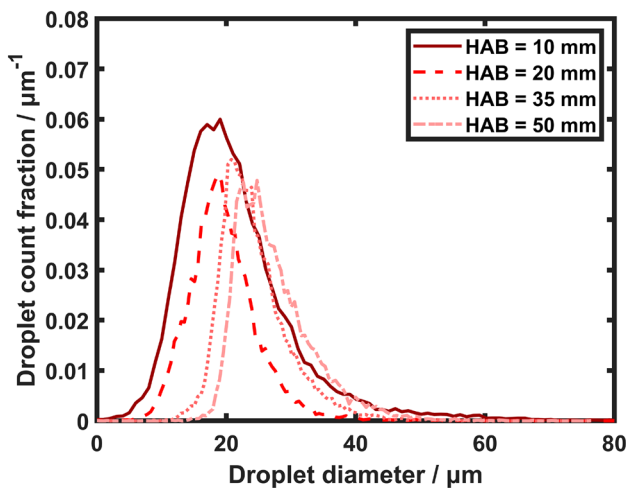


Fig. 6 Droplet count fraction as a function of height along the axial centerline of the flame spray for an ethanol feed rate of  $7.5 \text{ mL min}^{-1}$  and  $7.5 \text{ L min}^{-1}$  oxygen

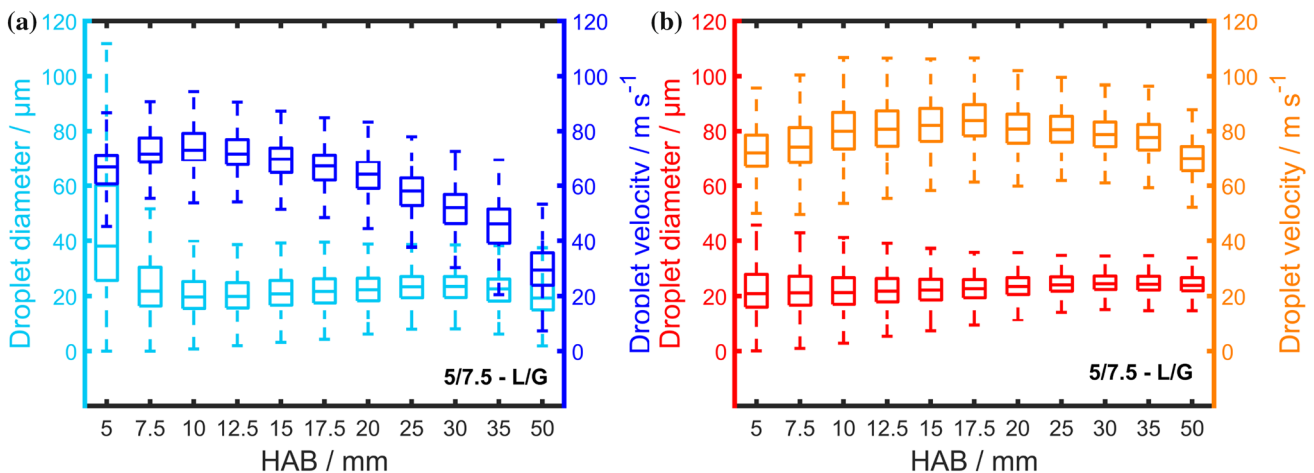


Fig. 7 Evolution of droplet mean diameter and droplet mean velocities along the axial centerline by PDA for an ethanol spray with a feed rate (L) of  $5 \text{ mL min}^{-1}$  and a dispersion gas flow (G) of  $7.5 \text{ L min}^{-1}$

found that the gas velocity is mainly affected by the feed rate under reacting conditions. Here, an increase of the feed rate from  $3$  to  $7.5 \text{ mL min}^{-1}$  results in a gas velocity reduction of up to  $20 \text{ m s}^{-1}$ . In contrast, in the cold spray, the gas velocity is not significantly affected by increasing the feed rate. This leads to the conclusion that the effect of the feed rate on the kinetic energy of the gas is rather low compared to the accelerating effect of rapid vapor release from ethanol. This lower gas flame velocities with increasing feed rate are consistent with the findings reported in the literature (Heine and Pratsinis 2005).

### 3.3.4 Flame spray turbulence

Figures 9 and 10 illustrate the radial mean velocity  $\bar{u}$ , turbulence intensity  $T_u$ , and the RMS velocity fluctuations  $u_{\text{RMS}}$  in radial and axial directions, respectively. For the prediction of turbulence scales, high effective data rates are necessary. When applying a feed rate of  $3 \text{ mL min}^{-1}$ , smaller droplets are detected in all regions of the spray. These smaller droplets have a smaller lifetime and no predictions of turbulence scales can be made for a feed rate of  $3 \text{ mL min}^{-1}$  at  $\text{HAB} > 35 \text{ mm}$  since droplet data rate drops owing to droplet evaporation. In both radial directions, the RMS velocity fluctuations  $u_{\text{RMS}}$  have a maximum at the position where the gradient of the droplet velocity and the gradient of the turbulence intensity are highest, i.e.,  $r \approx -3 \text{ mm}$  and  $r \approx 3 \text{ mm}$  at  $\text{HAB} = 25 \text{ mm}$ . This region of high shear rates in radial direction can be observed in Fig. 3 and links the jet core with the spray boundary, characterized by decaying mean droplet velocities and droplet concentration. Inside the jet core, a local minimum of  $u_{\text{RMS}}$  and  $T_u$  is observed, which is consistent with the literature (Muniz and Mungal 2001; Heine et al. 2006).

$\text{min}^{-1}$ . The boxes represent the 25th and 75th and the bars the 0.7th and 99.3th percentiles of the distribution, respectively. **a** Non-reacting conditions; **b** reacting conditions. Note that the x-axis is not linear

This might be caused by a deflection of small droplets from the centerline in radial direction as they easily follow the turbulent flow pattern.

In axial direction, the velocity fluctuations are mainly influenced by the rapid droplet acceleration in the nozzle near-field. Further downstream, a smooth decay in velocity fluctuations is observed owing to a decreasing droplet velocity magnitude and a slightly increasing droplet diameter (Fig. 5) that contributes to a reduced turbulence intensity  $T_u$ .

To understand the velocity dependence of turbulence scales within the flame spray, the normalized one-dimensional power spectral density (PSD) measured for different feed rates at HAB = 25 mm and for different distances to the nozzle tip at constant feed rate is illustrated in Fig. 11a, b, respectively. According to Kolmogorov's theory (Tennekes and Lumley 1972), the linear slope of  $-5/3$  in the inertial range indicates the isotropy of small turbulent scales, where energy conversion from larger to smaller flow structures takes place (Tennekes and Lumley 1972). As can be deduced from Fig. 11a, the influence of varying feed rates in the range of 3–7.5 mL min<sup>-1</sup> at constant dispersion gas pressure on the PSD is insignificant. In contrast, the PSD depends significantly on the distance to the nozzle tip. Figure 11b illustrates the power spectrum measured at two different positions on the axial centerline. In both spectra, the linear slope of  $-5/3$  in the inertial range is resolved clearly. However, a distinct negative shift in the source range of the PSD can be observed at increasing the distance to the nozzle. This decrease in the energy spectrum indicates a decreasing energy level of turbulence from HAB = 20 mm to HAB = 50 mm.

Figure 12 illustrates the predicted Kolmogorov shear rate  $\Gamma$  (solid line) and the Kolmogorov length scale  $\eta$  (dotted line) for the axial velocity component as a function of height. As already observed for the PSD function in Fig. 11,

the liquid feed rate does not significantly influence the turbulent flow pattern. The turbulence length scale  $\eta$  increases from 91  $\mu\text{m}$  up to more than 368  $\mu\text{m}$  (5-L) and 314  $\mu\text{m}$  (7.5-L). These decreasing length scales of turbulence are consistent with the decrease in turbulence intensity shown in Fig. 10. The observed length scale in the size range of 91–368  $\mu\text{m}$  is of the same order of magnitude compared to similar investigations with the Schlick external-mixing gas-assisted nozzle (Schlick-Düsen, Gustav Schlick GmbH + Co, 970/4-S32) reported by Heine et al. (2006). Heine et al. measured jet velocities up to 120–140 m s<sup>-1</sup> and deduced Kolmogorov lengths  $\eta$  from 100 to 180  $\mu\text{m}$  using a premixed CH<sub>4</sub>/O<sub>2</sub> flame. At HAB = 10 mm, the Kolmogorov shear rate  $\Gamma$  results in 48,000 s<sup>-1</sup> and is followed by an asymptotical decay to 5000 s<sup>-1</sup> at HAB = 50 mm. The Kolmogorov shear rate is of great importance since the size of turbulence scales

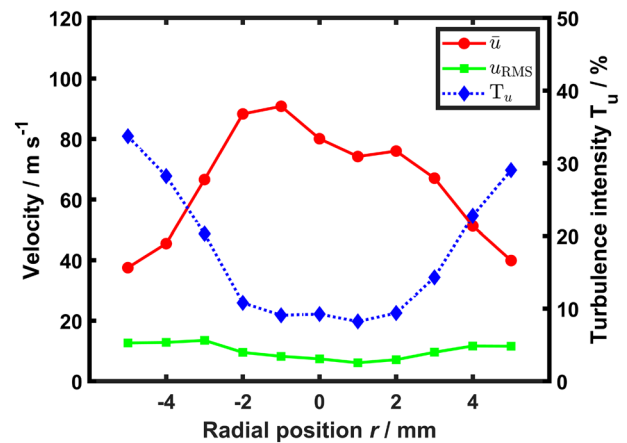


Fig. 9 Mean droplet velocity  $\bar{u}$ , RMS velocity fluctuation  $u_{RMS}$  and turbulence intensity  $T_u$  for a feed rate of 5 mL min<sup>-1</sup> and 7.5 L min<sup>-1</sup> dispersion gas as a function of distance to axial centerline measured at HAB = 25 mm

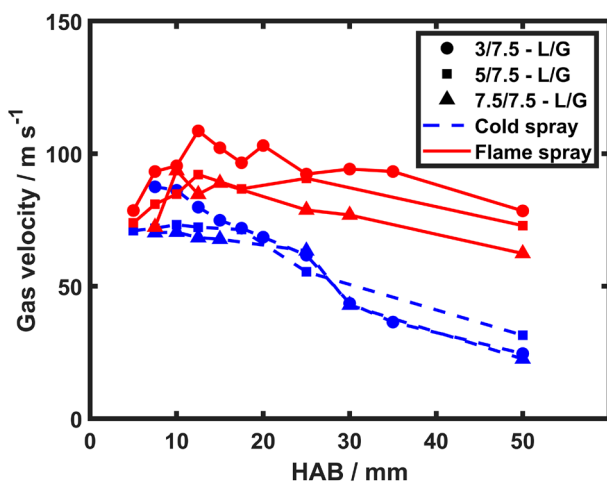


Fig. 8 Gas velocity along the axial centerline of the ethanol sprays

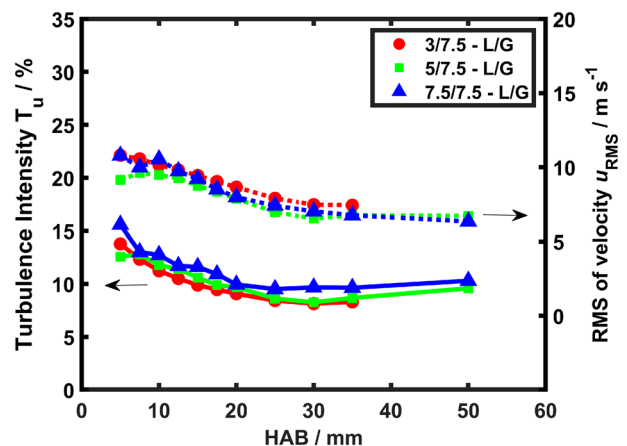


Fig. 10 Turbulence intensity  $T_u$  (solid line) and RMS velocity fluctuations  $u_{RMS}$  (dotted line) measured along the axial spray axis



is about one order of magnitude larger than the droplets and several order of magnitudes larger than flame spray-synthesized nanoparticles. Especially, the droplet and particle dynamics, such as coalescence, coagulation and fragmentation (Spicer and Pratsinis 1996), are strongly influenced by the shear stress and the intensified mixing of reactant and oxidizer significantly enhances reaction kinetics. According to Heine et al. (2006), shear rates of  $\Gamma = 1500 \text{ s}^{-1}$  can even cause the breaking of weak bonding between primary particles during particle agglomeration and consequently decrease the mean diameter of flame spray-synthesized nanopowder agglomerates.

### 3.3.5 Combustion mode

The burning rate of the droplets strongly depends on the combustion behaviour of droplets in groups. This group combustion behaviour can be characterized by the dimensionless group combustion number  $G$  (Chiu and Liu 1977), which can be interpreted as a Damkohler number associated with droplet combustion in spray flames (Chen and Gomez 1997). Chiu and Liu defined the group combustion number  $G$  as

$$G = 3(1 + 0.276Re^{0.5} Sc^{0.33})Le n^{2/3} \frac{d_d}{l}, \tag{8}$$

where  $Re$  is the droplet Reynolds number,  $Sc$  is the Schmidt number,  $Le$  is the Lewis number,  $n$  is the total number of droplets in the cloud,  $d_d$  is the droplet diameter, and  $l$  is the average spacing between single droplets (Chiu and Liu 1977). Since in practical studies on turbulent spray flames

like in this work the exact conditions specified in the definition of  $G$  are hard to quantify, simplifications must be made to estimate  $G$  from experimental PDA data. Chen and Gomez (1997) introduced a simplified group combustion number  $G$  neglecting the convective enhancement effect to the droplet evaporation, taking  $Le$  as unity and assuming a monodisperse cloud as

$$G = 2\pi\rho(n)d_dR_c^2, \tag{9}$$

where  $\rho(n)$  is the droplet number density and  $R_c$  is the cloud radius. While the droplet number density can be obtained from PDA measurements, the radius of the cloud  $R_c$  must be defined reasonably since  $G$  is quite sensitive to  $R_c$ . While different approaches to choose  $R_c$  adequately have been reported in the literature, a reasonable choice of  $R_c$  in the core region is the radius of the droplet-laden portion of the jet (Wark et al. 2000; Mädler et al. 2002). In this work,  $R_c$  is the radius of the jet core of the droplet-laden fraction deduced from LSMS recording as shown in Fig. 3. To visualize adequately the droplet-laden fraction and the spray front in the images, single LSMS images were averaged and then allowed to reach the threshold using the triangle approach implemented in ImageJ (Version 1.46r) (Zack et al. 1977). The jet core radius deduced from LSMS images for the investigated liquid feed rates are shown in Fig. 13. A representative choice of  $d_d$  for the droplet length scale is the arithmetic mean droplet diameter of the polydisperse system  $\bar{d}_d$  (Akamatsu et al. 1996; Mädler et al. 2002; Wark et al. 2000).

For  $1 \leq G \leq 100$ , the droplet combustion is governed by external group burning, with a slowly vaporizing droplet cloud surrounded by a vaporizing droplet sheath and a flame sheath as the spray boundary (Chiu and Liu 1977). The internal group regime, which is characterized by individually

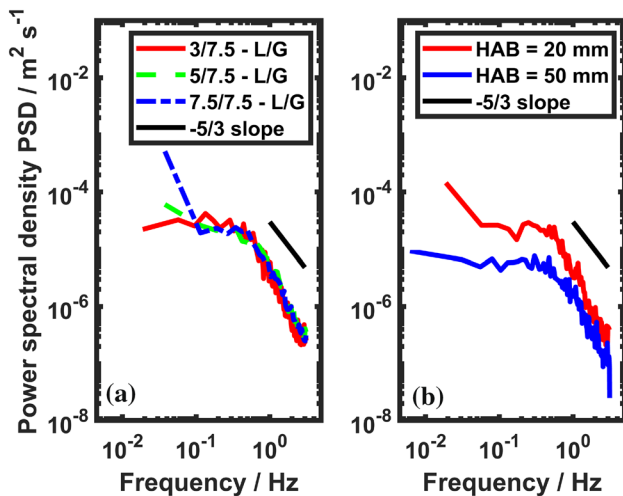


Fig. 11 **a** Power spectrum PSD of an ethanol flame spray for different ethanol feed rates measured at HAB = 25 mm. **b** Power spectrum of an ethanol flame spray with a feed rate of 7.5 mL min<sup>-1</sup> and 7.5 L min<sup>-1</sup> of dispersion gas

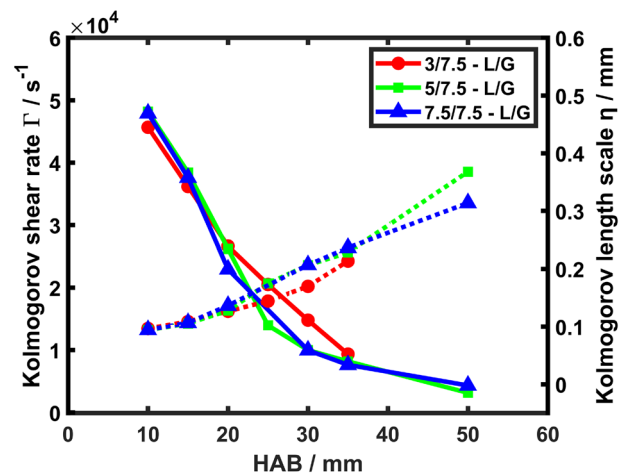


Fig. 12 Kolmogorov shear rate  $\Gamma$  (solid line) and Kolmogorov length scale  $\eta$  (dotted line) as a function of the distance from the nozzle tip

vaporizing and burning droplets, is identified for  $0.01 \leq G \leq 1$ . Isolated single droplet combustion, where single droplets vaporize and burn without interfering with neighboring droplets is described for  $G < 0.01$ . It is noteworthy that the droplet-laden jet core vanishes at  $HAB > 35$  mm as can be observed in Fig. 13. At larger HAB, for not evaporated droplets, which might be a result from non-vaporizing droplet clouds and/or droplets with larger initial diameter, the single droplet combustion mode may prevail owing to low droplet concentrations and large droplet spacing (see, for comparison, Fig. 4).

Figure 14 shows the evolution of the combustion number  $G$  with increasing HAB for different ethanol feed rates at a dispersion gas flow rate of  $7.5 \text{ mL min}^{-1}$  oxygen. As can be observed for small distances to nozzle tip, all investigated feed rates underlie group combustion numbers  $G$  of the order of 1, which is the boundary between external group and internal group combustion. This order of magnitude indicates that most of the droplets inside of the jet core close to the nozzle merely evaporate, while droplets at the boundaries of the spray core burn enclosing the core with individual flames. Also, increasing feed rates promote an increase of  $G$  and increasing HAB in streamwise direction leads to a significant reduction of  $G$ . This is owing to the higher droplet flux, the higher liquid mass to volume ratio for increased feed rates and the larger jet core radius  $R_c$  in regions close to the nozzle ( $HAB < 20$  mm). Especially, the latter is of importance, since the jet core radius can be reduced by large oxidizer/fuel ratios, which can promote internal group combustion (Mädler et al. 2002). The oxidizer/fuel ratios for the measurements using  $7.5 \text{ L min}^{-1} \text{ O}_2$  dispersion gas were 6.50, 3.90 and 2.60 for 3, 5, and  $7.5 \text{ mL min}^{-1}$  ethanol feed rates, respectively. The largest group combustion number  $G$  is reached applying a feed rate of  $7.5 \text{ mL min}^{-1}$  with  $G = 2.78$  since higher liquid feed rates result in a higher liquid mass per unit volume and thus in lower spacings. For HAB greater than 20 mm, the internal group combustion regime governs the sprays since the ongoing droplet evaporation decreases the droplet number density and enables most of the droplets to be surrounded by individual flames. Far away from the nozzle exit ( $HAB > 30$  mm), individual droplet combustion without interfering droplets is reached.

## 4 Conclusions

The droplet size distributions and velocity profiles of three different reacting and non-reacting ethanol sprays have been studied using PDA measurements, giving a deeper insight into mixing zones and turbulent flow fields of the SpraySynburner. The gas dynamics have been deduced from droplets of  $d_d < 4 \mu\text{m}$  and maximal gas velocities of  $110 \text{ m s}^{-1}$  have

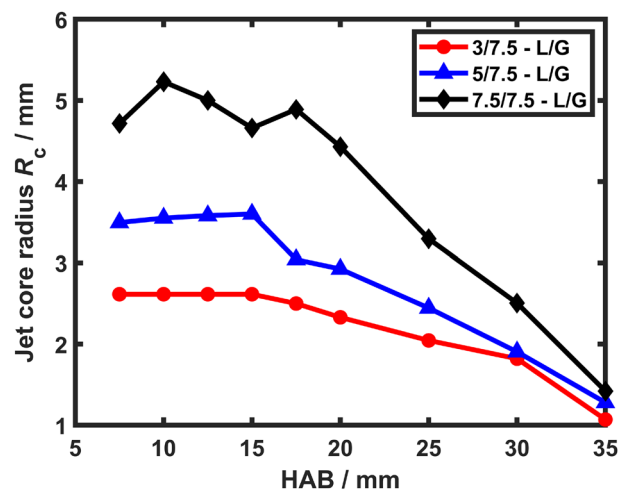


Fig. 13 Jet core radius  $R_c$  as a function of distance to nozzle tip for different ethanol feed rates

been measured. It was found that an increasing feed rate leads to lower droplet and gas velocities. Along the axial centerline, the droplet mean diameter increases due to rapid evaporation of small droplets. The Kolmogorov length scale  $\eta$  ( $100\text{--}363 \mu\text{m}$ ) and the Kolmogorov shear rate  $\Gamma$  ( $5000\text{--}48,000 \text{ s}^{-1}$ ) have been derived using axial velocity components. Both, length scale and shear rate were of the same order of magnitude as for similar FSP-burners (Heine et al. 2006). LSMS images revealed the jet morphology within the spray and traced the length of the dense spray region under reacting conditions. The group combustion model according to Chiu and Liu (1977) could be applied in a simplified form (Chen and Gomez 1997) using the jet core radius, derived from LSMS images, and PDA data. While for increased feed rates the external group combustion mode ( $G > 1$ ) prevails in regions close to nozzle tip, the mode

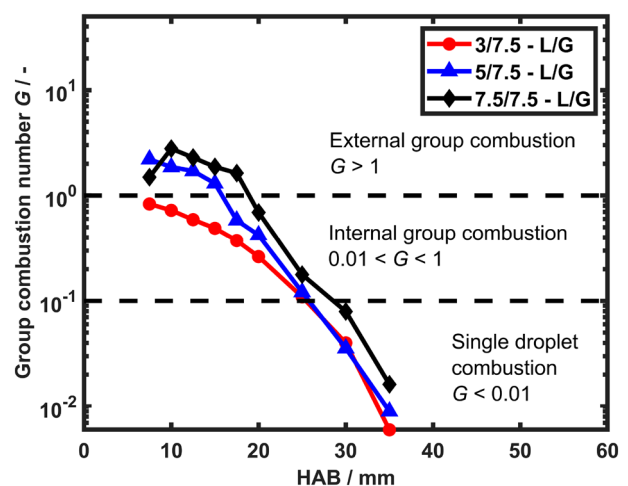


Fig. 14 Group combustion number  $G$  of an ethanol flame spray

switches for distances of  $HAB > 20$  mm to internal group combustion. In contrast, lower feed rates of  $3 \text{ mL min}^{-1}$ , even in regions very close to the nozzle exit, are governed by internal group combustion. For  $HAB > 30$  mm, the single droplet combustion mode, with individually evaporating droplets, is reached for all applied feed rates. This leads to the conclusion that larger feed rates favor the formation of burning clouds with slowly evaporating droplets that impede homogeneously developed mixing zones. The operation with small  $G$  numbers favors the formation of homogeneous mixing zones and, therefore, improves the combustion kinetics.

**Acknowledgements** The authors acknowledge F. Meierhofer, N. Riefler, and T. Wriedt for fruitful discussions and technical assistance. They also acknowledge financial support from the Deutsche Forschungsgemeinschaft (DFG) within the priority program SPP 1980 SPRAYSYN under Grants KI 1396/6-1 and FR 912/42-1.

## References

- Akamatsu F, Miutani Y, Katsuki M, Tsushima S, Cho YD (1996) Measurement of the local group combustion number of droplet clusters in a premixed spray stream. *Symp (Int) Combust* 26(1):1723–1729
- Bachalo WD (2000) Spray diagnostics for the twenty-first century. *At Sprays* 10(3–5):439–474
- Berrocal E (2006) Multiple scattering of light in optical diagnostics of dense sprays and other complex turbid media. Ph.D. thesis, Cranfield University
- Chao J, Rossini FD (1965) Heats of combustion, formation, and isomerization of nineteen alkanols. *J Chem Eng Data* 10(4):374–379
- Chen G, Gomez A (1997) Dilute laminar spray diffusion flames near the transition from group combustion to individual droplet burning. *Combust Flame* 110(3):392–404
- Chiu HH, Liu TM (1977) Group combustion of liquid droplets. *Combust Sci Technol* 17(34):127–142
- Coghe A, Cossali GE (2012) Quantitative optical techniques for dense sprays investigation: a survey. *Opt Lasers Eng* 50(1):46–56
- Eslamian M, Heine MC (2008) Characteristics of spray flames and the effect of group combustion on the morphology of flame-made nanoparticles. *Nanotechnology* 19(4):045712
- Gröhn AJ, Pratsinis SE, Wegner K (2012) Fluid-particle dynamics during combustion spray aerosol synthesis of zro2. *Chem Eng J* 191:491–502
- Hamid NA, Wennig S, Hardt S, Heinzl A, Schulz C, Wiggers H (2012) High-capacity cathodes for lithium-ion batteries from nanostructured lifepo4 synthesized by highly-flexible and scalable flame spray pyrolysis. *J Power Sources* 216:76–83
- Heine MC, Pratsinis SE (2005) Droplet and particle dynamics during flame spray synthesis of nanoparticles. *Ind Eng Chem Res* 44(16):6222–6232
- Heine MC, Mädler L, Jossen R, Pratsinis SE (2006) Direct measurement of entrainment during nanoparticle synthesis in spray flames. *Combust Flame* 144(4):809–820
- Kelesidis GA, Goudeli E, Pratsinis SE (2017) Flame synthesis of functional nanostructured materials and devices: surface growth and aggregation. *Proc Combust Inst* 36(1):29–50
- Lefebvre AH, McDonnell VG (2017) *Atomization and sprays*. CRC Press, Boca Raton
- Li H, Rosebrock CD, Riefler N, Wriedt T, Mädler L (2017) Experimental investigation on microexplosion of single isolated burning droplets containing titanium tetraisopropoxide for nanoparticle production. *Proc Combust Inst* 36(1):1011–1018
- Linne M, Paciaroni M, Berrocal E, Sedarsky D (2009) Ballistic imaging of liquid breakup processes in dense sprays. *Proc Combust Inst* 32(2):2147–2161
- Mädler L, Kammler HK, Mueller R, Pratsinis SE (2002) Controlled synthesis of nanostructured particles by flame spray pyrolysis. *J Aerosol Sci* 33(2):369–389
- Meierhofer F, Li H, Gockeln M, Kun R, Grieb T, Rosenauer A, Fritsching U, Kiefer J, Birkenstock J, Mädler L, Pokhrel S (2017) Screening precursor-solvent combinations for  $\text{Li}_4\text{Ti}_5\text{O}_{12}$  energy storage material using flame spray pyrolysis. *ACS Appl Mater Interfaces* 9(43):37760–37777
- Muniz L, Mungal MG (2001) Effects of heat release and buoyancy on flow structure and entrainment in turbulent nonpremixed flames. *Combust Flame* 126(1–2):1402–1420
- Petermann N, Stein N, Schierner G, Theissmann R, Stoib B, Brandt MS, Hecht C, Schulz C, Wiggers H (2011) Plasma synthesis of nanostructures for improved thermoelectric properties. *J Phys D Appl Phys* 44(17):174034
- Rosebrock CD, Wriedt T, Mädler L, Wegner K (2016) The role of microexplosions in flame spray synthesis for homogeneous nanopowders from low-cost metal precursors. *AIChE J* 62(2):381–391
- Schulz C, Dreier T, Fikri M, Wiggers H (2018) Gas-phase synthesis of functional nanomaterials: challenges to kinetics, diagnostics, and process development. *Proc Combust Inst* 37(1):83–108
- Sehlleier YH, Hardt S, Schulz C, Wiggers H (2016) A novel magnetically-separable porous iron-oxide nanocomposite as an adsorbent for methylene blue (mb) dye. *J Environ Chem Eng* 4(4):3779–3787
- Sirignano WA (1983) Fuel droplet vaporization and spray combustion theory. *Prog Energy Combust Sci* 9(4):291–322
- Sirignano WA, Mehring C (2000) Review of theory of distortion and disintegration of liquid streams. *Prog Energy Combust Sci* 26(4–6):609–655
- Sornek RJ, Dobashi R, Hirano T (2000) Effect of turbulence on vaporization, mixing, and combustion of liquid-fuel sprays. *Combust Flame* 120(4):479–491
- Spicer PT, Pratsinis SE (1996) Coagulation and fragmentation: universal steady-state particle-size distribution. *AIChE J* 42(6):1612–1620
- Strakey PA, Talley DG, Sankar SV, Bachalo WD (2000) Phase-doppler interferometry with probe-to-droplet size ratios less than unity I. Trajectory errors. *Appl Opt* 39(22):3875–3886
- Teja AS, Koh PY (2009) Synthesis, properties, and applications of magnetic iron oxide nanoparticles. *Prog Cryst Growth Charact Mater* 55(1–2):22–45
- Tennekes H, Lumley JL (1972) *A first course in turbulence*. MIT press, Cambridge
- Tikkanen J, Gross KA, Berndt CC, Pitkänen V, Keskinen J, Raghu S, Rajala M, Karthikeyan J (1997) Characteristics of the liquid flame spray process. *Surf Coat Technol* 90(3):210–216
- Wark C, Eickmann K, Richards C (2000) The structure of an acoustically forced, reacting two-phase jet. *Combust Flame* 120(4):539–548
- Zack GW, Rogers WE, Latt SA (1977) Automatic measurement of sister chromatid exchange frequency. *J Histochem Cytochem* 25(7):741–753

**Publisher's Note** Springer Nature remains neutral with regard to jurisdictional claims in published maps and institutional affiliations.